



Understanding the Mass, Momentum and Energy Transfer in the Frozen Soil with Three Levels of Model Complexities

Lianyu Yu¹, Yijian Zeng¹, Zhongbo Su^{1,2}

5 ¹Faculty of Geo-information and Earth Observation (ITC), University of Twente, Enschede, The Netherlands

²Key Laboratory of Subsurface Hydrology and Ecological Effect in Arid Region of Ministry of Education, School of Water and Environment, Chang'an University, Xi'an, China

Correspondence to: Yijian Zeng (y.zeng@utwente.nl); Zhongbo Su (z.su@utwente.nl)

Abstract

10 Frozen ground covers vast area of earth surface and has its important ecohydrological implications for high latitude and high altitude regions under changing climate. However, it is challenging to characterize the simultaneous transfer of mass and energy in frozen soils. Within the modeling framework of STEMMUS (Simultaneous Transfer of Mass, Momentum and Energy in Unsaturated Soil), the model complexity of soil heat and mass transfer varies from uncoupled, to coupled heat and mass transfer, and further to the explicit
15 consideration of airflow (termed as unCPLD, CPLD, and CPLD-AIR, respectively). The impact of different model complexities on understanding the mass, momentum and energy transfer in frozen soil were investigated. The model performance in simulating water and heat transfer and surface latent heat flux was tested on a typical Tibetan Plateau meadow. Results indicate that the CPLD model considerably improved the simulation of soil moisture, temperature and latent heat flux. The analyses of heat budget reveal that the
20 improvement of soil temperature simulations by CPLD model is ascribed to its physical consideration of vapor flow and thermal effect on water flow, with the former mainly functions above the evaporative front and the latter dominates below the evaporative front. The contribution of airflow-induced water and heat transport to the total mass and energy fluxes is negligible. Nevertheless, given the explicit consideration of airflow, vapor flow transfer and its effect on heat transfer were enhanced during the freezing-thawing
25 transition period.



1. Introduction

Frozen soils, have been reported with significant changes under climate change (Cheng and Wu, 2007;Hinzman et al., 2013;Zhao et al., 2019). Changes in freezing/thawing process can alter soil hydrothermal regimes, activate/close the water flow pathways and vegetation development (Walvoord and Kurylyk, 2016). Such changes will further considerably affect the spatial pattern, the seasonal to interannual variability and long term trends in land surface water, energy and carbon budgets and then the land surface atmosphere interactions (Schuur et al., 2015;Subin et al., 2013;Walvoord and Kurylyk, 2016). Understanding the soil freeze/thaw processes appears to be the necessary path to the better water resources management and ecosystem protection in cold regions.

When soil experiences the freeze/thaw process, there is a dynamic thermal equilibrium system of ice, liquid water, water vapor and dry air in soil pores. Water and heat flow are tightly coupled in frozen soils. Coupled water and heat physics, describing the concurrent flow of liquid, vapor as well as heat flow, was first proposed by Philip and De Vries (1957), (hereafter termed as PdV57) considering the enhanced vapor transport. The PdV57 theory has been widely applied for detailed understanding of soil evaporation during the drying process (De Vries, 1958;De Vries, 1987;Milly, 1982;Novak, 2010;Saito et al., 2006). The attempts to simulate the coupled water and heat transport in frozen soils started in 1970s (e.g., Guymon and Luthin, 1974;Harlan, 1973). Since then, numerical tools able to and subjected to simulate one dimensional frozen soil were increasingly developed. Flerchinger and Saxton (1989) developed the SHAW model with the capacity of simulating the coupled water and heat transport process. Hansson et al. (2004) accounted for the phase changes in HYDRUS-1D model and verified its numerical stability with rapidly changing boundary conditions. Considering the two components (water and gas) and three water phases (liquid, vapor, and solid), Painter (2011) developed a fully coupled water and heat transport model MarsFlo. These works together with other modifications, simplifications, generate a series of hierarchy of frozen soil models (detail reviewed by Li et al., (2010) and Kurylyk and Watanabe (2013)).

Air flow has been reported important to the soil water and heat transfer process under certain conditions (Prunty and Bell, 2007;Touma and Vauclin, 1986). Zeng et al., (2011a, b) found that soil evaporation is enhanced after precipitation events by considering air flow and demonstrated that the air pressure induced advective fluxes inject the moisture into the surface soil layers and increase the hydraulic conductivity at top layer. The diurnal variations of air pressure resulted in the vapor circulation between the atmosphere and land surface. Wicky and Hauck (2017) reported that the temperature difference between the upper and the lower part of a permafrost talus slope was significant and attributed it to the airflow induced convective heat flux. Yu et al., (2018) analyzed the spatial and temporal dynamics of air pressure induced fluxes and found an interactive effect as the presence of soil ice. The abovementioned studies demonstrate that the explicit consideration of air flow has the potential to affect the soil hydrothermal regime.



60 Current land surface models (hereafter LSMs), however, usually adopted a simplified frozen soil physics
with relative coarse vertical discretization (Koren et al., 1999; Niu et al., 2011; Swenson et al., 2012; Viterbo
et al., 1999). In their parameterizations, soil water and heat interactions can only be indirectly activated by
the phase change processes, the mutual dependence of liquid water, water vapor, ice and dry air in soil pores
is of course absent. This mostly lead to unrealistic physical interpretations and worse performance regarding
65 to the hydrothermal, ecohydrological dynamics (Cuntz and Haverd, 2018; Novak, 2010; Wang and Yang,
2018). Specifically, Su et al. (2013) evaluated the European Centre for Medium-Range Weather Forecasts
(ECMWF) soil moisture analyses on the Tibetan Plateau, with HTESSEL as the land surface modelling
component. Their results indicated the deficiency of HTESSEL in capturing phase transitions. How and to
what extent the complex mutual dependence physics affects the soil mass and energy transfer in frozen soils?
70 Is it necessary to consider such a fully physical mechanism in LSMs? These two questions frame the scope
of this work.

In this paper, we incorporated the various complexity of water and heat transport mechanisms into a common
modeling framework (STEMMUS-FT, Simultaneous Transfer of Energy, Momentum and Mass in
Unsaturated Soils with Freeze-Thaw). With the aid of in situ measurements collected from a typical Tibetan
75 meadow site, the pros and cons of different model complexities were investigated. Subsurface energy budgets
and latent heat flux density analyses were further conducted to illustrate the underlying mechanisms
considering different coupled water-heat physics. Section 2 describes the experimental site and the
implementation of increasing complexity of subsurface physics into STEMMUS framework. Performance of
different models is presented in Section 3 together with the subsurface heat budgets and latent heat flux
density analyses. Section 4 discusses the effects of considering coupled water-heat transport and air flow in
80 frozen soils. Conclusion is made in Section 5.

2. Methodology

2.1 Experimental site

Maqu station, equipped with a catchment scale soil moisture and soil temperature (SMST) monitoring
85 network and micro-meteorological observing system (Dente et al., 2012; Su et al., 2011; Zeng et al., 2016), is
situated on the north-eastern fringe of the Tibetan Plateau (33°30'–34°15'N, 101°38'–102°45'E). According
to the updated Köppen-Geiger climate classification system, it can be characterized as a cold climate with
dry winter and warm summer (Dwb). The mean annual air temperature is 1.2 °C, and the mean air
temperatures of the coldest month (January) and warmest month (July) are about -10.0 °C and 11.7 °C,
90 respectively. Alpine meadows (e.g., *Cyperaceae* and *Gramineae*), with heights varying from 5 cm to 15 cm
throughout the growing season, are the dominant land cover in this region. The sandy loam and silt loam are
found by in situ soil sampling and organic soil with a maximum of 18.3 % organic matter for the upper soil
layers (Dente et al., 2012; Zhao et al., 2018; Zheng et al., 2015).



95 The Maqu SMST monitoring network spans an area of approximately 40 km×80 km with the elevation
ranging from 3200 m to 4200 m a.s.l. SMST profiles are automatically measured by 5TM ECH₂O probes
(METER Group, Inc., USA) installed at the soil depths of 5 cm, 10 cm, 20 cm, 40 cm, and 80 cm. The micro-
meteorological observing system includes a 20 m Planetary Boundary Layer (PBL) tower providing the
meteorological measurements at five heights above ground (i.e., wind speed and direction, air temperature
and relative humidity) , and an eddy-covariance (EC150, Campbell Scientific, Inc., USA) system installed
100 for measuring the turbulent sensible, latent heat fluxes and carbon fluxes. Four component down and
upwelling solar and thermal radiation (NR01-L, Campbell Scientific, Inc., USA), and liquid precipitation
(T200B, Geonor, Inc., USA) are also monitored.

2.2 Mass and energy transport in unsaturated soils

On the basis of STEMMUS modelling framework, the increasing complexity of vadose zone physics in
105 frozen soils was implemented as three alternative models (Table 1). Firstly, STEMMUS enabled the
isothermal water and heat transfer physics (Eqs. 1 & 2). The 1-D Richards equation is utilized to solve the
isothermal water transport in variably saturated soils. The heat conservation equation took into account the
freezing/thawing process and the latent heat due to water phase change. The effect of soil ice on soil hydraulic
and thermal properties was considered. It is termed as unCPLD model.

110 Secondly, the fully coupled water and heat physics, i.e., water vapor flow and thermal effect on water flow,
was explicitly considered in STEMMUS, termed as CPLD model. For the CPLD physics, the extended
version of Richards (1931) equation with modifications made by Milly (1982) was used as the water
conservation equation (Eq. 3). Water flow can be expressed as liquid and vapor fluxes driven by temperature
gradient and matric potential gradient, respectively. The heat transport in frozen soils mainly includes: heat
115 conduction ($CHF, \lambda_{eff} \frac{\partial T}{\partial z}$), convective heat transferred by liquid flux ($CFL, -C_L q_L (T - T_r), -C_L S (T - T_r)$),
vapor flux ($CFV, -[L_0 q_V + C_V q_V (T - T_r)]$), the latent heat of vaporization (LHF, $\rho_V \theta_V L_0$), the latent
heat of freezing/thawing ($-\rho_i \theta_i L_f$) and a source term associated with the exothermic process of wetting of
a porous medium (integral heat of wetting) ($-\rho_i W \frac{\partial \theta_L}{\partial t}$). It can be expressed as Eq. 4 (De Vries 1958;
Hansson et al. 2004).

120 Lastly, STEMMUS expressed the freezing soil porous media as the mutual dependence system of liquid
water, water vapor, ice water, dry air and soil grains, in which the air flow was independently considered
while the other keep the same as CPLD model, termed as CPLD-AIR model (Eqs. 5, 6, & 7, Zeng et al.
2011a,b; Zeng and Su, 2013). The air flow induced water and vapor fluxes (q_{La}, q_{Va}) and its corresponding
convective heat flow ($CFa, q_a C_a (T - T_r)$) were involved in the water and heat transfer mechanisms,
125 respectively.



To accommodate the specific conditions of a Tibetan meadow, the total depth of soil column was set as 1.6 m. The vertical soil discretization was designed finer in the upper soil layers (0.1-2.5cm for 0-40cm) than that in the lower soil layers (5-20cm for 40-160cm). Three aforementioned models adopted the same set of soil parameters, shown as Table 2.

3. Results

Given by the same atmospheric forcing and same set of parameters, the performance of models with various complexity of unsaturated soil water and heat physics was illustrated as Sect. 3.1, 3.2 & 3.3. Sect. 3.4 & 3.5 further analyzed the variations of heat budgets and subsurface latent heat flux density, intended to present the underlying differences among various models.

3.1 Soil hydrothermal profile simulations

The performance of model with various soil physics in simulating the soil thermal profile information is illustrated in Fig. 1. Both CPLD and CPLD-AIR model well reproduced the time series of soil temperature at different soil depth except for the 40cm, which is probably due to the inappropriate measurements (e.g., improper placement of sensors). However, there are significant discrepancies of soil temperature simulated by the unCPLD model. Compared to the observations, a stronger diurnal behavior of soil temperature in response to the fluctuating atmospheric forcing was found and the earlier stepping in/stepping out of the frozen period was reproduced by the unCPLD model. Such differences enlarged at deeper soil layers with large BIAS and RMSE values (Table 3).

Figure 2 presents the time series of observed and model simulated soil liquid water content at five soil layers. During the rapid freezing period, a noticeable overestimation of diurnal fluctuations and early and fast decreasing of soil liquid water content was simulated by unCPLD model. Moreover, the strong diurnal fluctuations and early increase of liquid water content were also found during the thawing period. The early thawing of soil water even lead to an unrealistic refreezing process at 80 cm (from 88th to 92th day after December 2015), which is due to the simulated early warming of soil by unCPLD model (Fig. 1). Such discrepancies were significantly ameliorated from CPLD and CPLD-AIR simulations. Nevertheless, all three models can well capture the diurnal variations and magnitude of liquid water content during the frozen period. Note that there is an observable difference between CPLD and CPLD-AIR simulated soil liquid water content at shallower soil layers during the thawing process (e.g., Fig. 2, 5cm).

3.2 Freezing front propagation

The time series of freezing front propagation derived from the measured and model simulated soil temperature was reproduced as Figure 3. Initialized from the soil surface, the freezing front quickly develops downwards till the maximum freezing depth. The thawing process starts from both the top and bottom, mainly driven by the atmospheric heat and geothermal heat source, respectively. Such characteristics were well



160 captured by both the CPLD and CPLD-AIR model in terms of freezing rate, maximum freezing depth and
surface thawing process. While the unCPLD model tended to present a more fluctuated and rapid freezing
front propagation and a deeper maximum freezing depth which is early reached. The effect of atmospheric
heat source on soil temperature was overestimated by the unCPLD model as shown by the stronger diurnal
early onset of the thawing process.

165 **3.3 Surface Evapotranspiration**

The performance of model with different soil physics in reproducing the latent heat flux dynamics is shown
in Fig. 4. Compared to the observed LE, there is a significant overestimation of half-hourly latent heat flux,
which significantly degraded the overall performance using unCPLD model. The occurrence of such
overestimation was notably reduced using CPLD and CPLD-AIR model. While the general underestimation
170 of latent heat flux by the CPLD and CPLD-AIR model was found mostly during the freezing-thawing
transition period (Fig. 5b), when the soil hydrothermal states are not well captured (Fig. 1 &2).

The overestimation of surface evapotranspiration by unCPLD model was significant during the initial
freezing and freezing-thawing transition period (Fig. 5a, December & February). During the rapid freezing
period (January), unCPLD model presented a good match in the diurnal variation compared to the
175 observations. The monthly average diurnal variations were found to be well captured by CPLD and CPLD-
AIR models. Figure 5b shows the comparison of observed and model simulated cumulative surface
evapotranspiration. The overall overestimation of surface evapotranspiration by unCPLD model can be
clearly seen in Fig. 5b. Days at the initial freezing periods, with high liquid water content simulations,
accounted for more than 90% of the overestimation. The initial stage overestimation of surface
180 evapotranspiration was significantly reduced by CPLD and CPLD-AIR simulations. Slight underestimation
of cumulative surface evapotranspiration was simulated by CPLD and CPLD-AIR model with values of 3.98%
and 4.78%, respectively.

3.4 Heat budgets

Figure 6 shows the time series of the model simulated energy budget components at 5cm using unCPLD,
185 CPLD and CPLD-AIR during the freezing period (5th - 11th day after 1 December) and freezing-thawing
transition period (83th - 89th day after 1 December). For the unCPLD model, only the rate of change of heat
content HC and conductive heat flux divergence CHF are considered as the LHS and RHS of Eq. 2. Three
additional terms, convective heat flux divergence of liquid flow HFL and vapor flow HFV, and latent heat
flux divergence were included for the CPLD model. While for the CPLD-AIR model, the convective heat
190 flux divergence of air flow HFa was further added. There is a strong diurnal variation of heat budget
components (HC, CHF & LHF), corresponding to the diurnal fluctuation of soil temperature. For the unCPLD
model, the rate of change of heat content is almost completely balanced by the conductive heat flux
divergence CHF, indicating an acceptably accurate simulation. Compared to the unCPLD model, a stronger
diurnal fluctuation of HC and CHF, characterized as larger maximum/minimum heat budget component



195 values, was found in CPLD model results. Rendered from results of Fig. 1, the time series of the first order
of soil temperature regarding to time ($\partial T/\partial t$) simulated by unCPLD model was larger than that simulated
by CPLD model. This indicates unCPLD model produced a series of less fluctuations of apparent heat
capacity term ($C_{app} = C_{soil} + \rho_i \frac{L_f^2}{gT} \frac{d\theta}{d\psi}$) than CPLD models. During the freezing period, the latent heat flux
divergence LHF was lower than conductive heat flux divergence CHF by 1-2 orders of magnitude. The
200 positive value of LHF term during daytime indicates condensation happens at 5cm, as water vapor moves
downward (see Yu et al. (2018)). The convective heat fluxes of liquid flow and vapor flow was even smaller
compared to conductive heat flux. There is no significant difference of heat budget components between
CPLD and CPLD-AIR model in terms of diurnal variation and magnitude. The convective heat flux
divergence of air flow played a negligible role on the change of thermal state (HC).

205 The dynamics of heat balance components at 5 cm soil layer was tested for the freezing-thawing transition
period (Fig. 6 d, e, f). Both HC and CHF underwent strong diurnal variations with increasing fluctuation
magnitude, indicating soil temperature at 5 cm started warming. For the CPLD model, CHF exceeds HC
during daytime and the difference increased with time. Negative values were found for LHF and developed
further over time. The CHF and LHF terms summed to nearly balance the HC term. Such behavior was
210 similarly reproduced by CPLD-AIR model with a slightly large difference between HC and CHF terms. This
means larger amount of water vapor was evaporated from 5 cm soil layer (with more negative LHF term)
from CPLD-AIR simulations than that from CPLD simulations, which explains the lower liquid water content
for CPLD-AIR model (Fig. 2, 5 cm).

3.5 Subsurface latent heat flux density

215 To give more context to the results, the spatial and temporal distribution of model simulated latent heat flux
density (S_h), $-\rho_w L \partial q_v / \partial z$, during the freezing and freezing-thawing transition period was shown as Fig. 7.
For the unCPLD model, the latent heat flux density (S_h) is not available due to its inability to depict the vapor
flow process.

Figure 7a shows that there is a strong diurnal variation of S_h at upper 0.1cm soil layers. Such diurnal behavior
220 along the soil profile was interrupted by soil layer of 1cm, at which the water vapor consistently moved
upwards as evaporation source (termed as evaporative front). The path of this upward water vapor ended at
soil depth of 20cm from the 6th of December, where the freezing front developed. Compared to the upper
0.1cm soil, a weaker diurnal fluctuations of S_h was found at lower soil layers. For CPLD-AIR model, the
vapor transfer patterns are similar to that of CPLD model (Fig. 6b). There were isolated connections of
225 condensed water vapor between upper 1cm soil and the lower soil layers ($S_h > 0$, e.g., 6th, 7th, 9th, and 10th
of December), possibly associated with the downward air flow (see Fig. 12 in Yu et al. (2018)). The large
difference in magnitude of latent heat flux density between CPLD and CPLD-AIR model appeared mainly
isolated at upper soil layers (Fig. 7c). At soil layers between 1cm and 20cm, CPLD-AIR model simulated
less in condensation vapor area ($S_h > 0$) and more in the evaporation area ($S_h < 0$), indicating that CPLD-AIR



230 model produced an additional amount of condensation and evaporation water vapor compared with CPLD
model (Fig. 7c).

Similar to that during the freezing period, strong diurnal variations at upper soil layers, interruption of diurnal
patterns by the constant upward evaporation of intermediate soil layers, and weak diurnal variation at lower
soil layers of S_h can be clearly observed along soil profile during the freezing-thawing transition period (Fig.
235 7d, e). While the maximum evaporation rate was less than that during the freezing period. The consistent
evaporation zone developed to a depth of 5 cm. The path for the upwards water vapor tended to develop
deeper than 30cm with the absence of soil ice. The simulation by CPLD-AIR model produced more
condensation and less evaporation water vapor than that by CPLD model can be seen more clearly (Fig. 7f).
In addition, steadily more evaporation water vapor from soil depth of 5 cm was simulated by CPLD-AIR
240 model compared to CPLD model. This confirms the aforementioned point that during the freezing-thawing
transition period, large LHF values were simulated by CPLD-AIR model (Fig. 6).

4. Discussion

4.1 Coupled Water and Heat Transfer Processes

The coupled water and heat transfer is realized via considering the vapor transfer processes. The mutual
245 dependence of soil water, in different phases (liquid, water vapor, and ice), and heat transport is enabled to
facilitate our better understanding of the complex soil physical processes (e.g., Fig. 6-7). Specifically, the
coevolution of soil moisture and soil temperature (SMST) profiles simulated by CPLD model was closer to
the observation than that by unCPLD model. In addition, significant enhancement in portraying the monthly
average diurnal variations of surface evapotranspiration and cumulative evapotranspiration can be found
250 from CPLD model simulations, which constraints the hydrothermal regimes especially during the freezing-
thawing transition periods (Fig. 1, 2& 5). During the freezing period, liquid water in the soil freezes, which
is analog to the soil drying process, and water vapor fluxes instead of liquid fluxes dominate the mass transfer
process. Neglecting such important water flux component unavoidably results in unrealistic simulations of
surface evapotranspiration and SMST profiles. From the energy budget perspective, the contribution of vapor
255 fluxes to the heat balance budget is more evidenced at soil layers above the evaporative front than that below
it (e.g., Fig. 6a vs. Fig. 6d, corresponding evaporative front shown as Fig. 7a vs. Fig. 7d). The downward
latent heat flux from CPLD model makes the subsurface soil warmer, which reduces the temperature gradient
($\partial T/\partial z$). This further results in the weaker diurnal fluctuations of conduction term for CPLD model than that
for the unCPLD model (Fig. 6). At the soil layers below the evaporative front, the heat flux source from
260 vapor diffusion process (LHF) is negligible. Thermal retard effect as the presence of soil ice, expressed as
the apparent heat capacity term (C_{app}), dominates the heat transfer process in frozen soils. CPLD model,
considering the thermal effect on water flow, usually has a larger water capacity value $\partial\theta/\partial\psi$ than unCPLD
model. As such, the intense thermal impedance effect leads to the results that CPLD model has a weaker
diurnal fluctuation of soil temperature than unCPLD model at subsurface soil layers.



265 **4.2 Air Flow in the Soil**

Since soil pores are filled with liquid water, vapor and dry air, taking dry air as an independent state variable can facilitate better understanding of the relative contribution of each component in soil pores to the mass and heat transfer in soils. The results show that the dry air-induced water and heat flow is negligible to the total mass and energy transfer (Yu et al., 2018; Zeng et al., 2011a). Nevertheless, dry air can affect soil hydrothermal regimes significantly under certain circumstances. Wicky and Hauck (2017) reported that the airflow-induced convective heat transfer resulted in a considerable temperature difference between the upper and lower part of a permafrost talus slope and thus have a remarkable effect on the thermal regime of the talus slope. Zeng et al. (2011a) demonstrated the airflow-induced surface evaporation enhanced after precipitation events, since the hydraulic conductivity of topsoil layers increased tremendously due to the airflow from the atmosphere into the soil. In this study, we found that the explicit consideration of airflow have the model produce an additional amount of subsurface condensation and evaporative water vapor in the condensation region and evaporation region, respectively (Fig. 7c & f). The effect of latent heat flux on heat transfer was enhanced by airflow during the freezing-thawing transition period (Fig. 6), which further affects the subsurface hydrothermal simulations (e.g., Fig. 2).

280 **5. Conclusions**

On the basis of STMMUS modeling framework with various complexity of water and heat transfer physics (unCPLD, CPLD and CPLD-AIR model), the performance of each model in simulating water and heat transfer and surface evapotranspiration was tested on a typical Tibetan meadow. Results indicate that compared to the in situ observations, the unCPLD model tended to present an earlier freezing and thawing date with a stronger diurnal variation of soil temperature/liquid water in response to the atmospheric forcing. Such discrepancies were considerably reduced by model with the coupled water-heat physics. Surface evapotranspiration was overestimated by unCPLD model, mainly due to the mismatches during the initial freezing and freezing-thawing transition period. CPLD models, with the coupled constraints from the perspective of water and energy conservation, significantly improve the model performance in mimicking the surface evapotranspiration dynamics during frozen period. The analysis of heat budget components and latent heat flux density revealed that the improvement of soil temperature simulations by CPLD model is ascribed to its physical consideration of vapor flow and thermal effect on water flow, with the former mainly functions at regions above the evaporative front, the latter dominates below the evaporative front. The contribution of airflow induced water and heat flow to the total mass and energy fluxes is negligible. However, given the explicit consideration of airflow, the latent heat flux and its effect on heat transfer were enhanced during the freezing-thawing transition period. This work highlighted the role of considering the vapor flow, thermal effect on water flow, and airflow in portraying the subsurface soil hydrothermal dynamics especially during freezing-thawing transition periods. To sum up, this study can contribute to a better understanding of freeze-thaw mechanisms of permafrost, which will subsequently contribute to the quantification of



300 permafrost carbon feedback (Burke et al., 2013; Schaefer et al., 2014; Schuur et al., 2015), if the STEMMUS-
FT model is to be coupled with a biogeochemical model, as lately implemented (Yu et al., 2020).

Data availability. The soil hydraulic/thermal property data can be freely downloaded from 4TU. Center for
Research Data (<https://doi.org/10.4121/uuid:61db65b1-b2aa-4ada-b41e-61ef70e57e4a>). Some relevant data
305 are made available from 4TU. Center for Research Data ([https://doi.org/10.4121/uuid:cc69b7f2-2448-
4379-b638-09327012ce9b](https://doi.org/10.4121/uuid:cc69b7f2-2448-4379-b638-09327012ce9b)).

Author contribution. Conceptualization, Z.S. and Y.Z.; methodology, L.Y., Y.Z.; writing - original draft
preparation, L.Y., Y.Z.; writing – review & editing, L.Y., Y.Z., Z.S..

310

Competing interests. The authors declare that they have no conflict of interest.

Acknowledgment

This work is supported by the National Natural Science Foundation of China (grant no. 41971033) and
315 supported by the Fundamental Research Funds for the Central Universities, CHD (grant no. 300102298307).
The authors thank the editor and referees very much for their constructive comments on improving the
manuscript.



Notation

Parameter	Symbol	Unit	Value
Volumetric water content	θ	$\text{m}^3 \text{m}^{-3}$	
Water flux	q	$\text{kg m}^{-2} \text{s}^{-1}$	
Vertical space coordinate (positive upwards)	z	m	
Sink term for transpiration, evaporation	S	s^{-1}	
Density of soil liquid water	ρ_L	kg m^{-3}	1000
Hydraulic conductivity	K	m s^{-1}	
Water potential	ψ	m	
Time	t	s	
Heat capacity of the bulk soil	C_{soil}	$\text{J kg}^{-1} \text{°C}^{-1}$	
Soil temperature	T	°C	
Effective thermal conductivity of the soil	λ_{eff}	$\text{W m}^{-1} \text{°C}^{-1}$	
Latent heat of fusion	L_f	J kg^{-1}	3.34E5
Soil ice volumetric water content	θ_i	$\text{m}^3 \text{m}^{-3}$	
Density of water vapor	ρ_v	kg m^{-3}	
Density of ice	ρ_i	kg m^{-3}	920
Soil liquid volumetric water content	θ_L	$\text{m}^3 \text{m}^{-3}$	
Soil vapor volumetric water content	θ_v	$\text{m}^3 \text{m}^{-3}$	
Soil liquid water fluxes (positive upwards)	q_L	$\text{kg m}^{-2} \text{s}^{-1}$	
Soil water vapor fluxes (positive upwards)	q_v	$\text{kg m}^{-2} \text{s}^{-1}$	
Isothermal hydraulic conductivities	K_{Lh}	m s^{-1}	
Thermal hydraulic conductivities	K_{LT}	$\text{m}^2 \text{s}^{-1} \text{°C}^{-1}$	
Isothermal vapor conductivity	D_{vh}	$\text{kg m}^{-2} \text{s}^{-1}$	
Thermal vapor diffusion coefficient	D_{vT}	$\text{kg m}^{-1} \text{s}^{-1} \text{°C}^{-1}$	
Specific heat capacity of soil solids	C_s	$\text{J kg}^{-1} \text{°C}^{-1}$	
Specific heat capacity of liquid	C_L	$\text{J kg}^{-1} \text{°C}^{-1}$	4.186
Specific heat capacity of water vapor	C_v	$\text{J kg}^{-1} \text{°C}^{-1}$	1.87
Specific heat capacity of ice	C_i	$\text{J kg}^{-1} \text{°C}^{-1}$	2.0455
Density of solids	ρ_s	kg m^{-3}	
Volumetric fraction of solids in the soil	θ_s	$\text{m}^3 \text{m}^{-3}$	
Arbitrary reference temperature	T_r	°C	20



Latent heat of vaporization of water at the reference temperature	L_o	J kg^{-1}	
Differential heat of wetting	W	J kg^{-1}	
Liquid water flux driven by the gradient of matric potential	q_{Lh}	$\text{kg m}^{-2} \text{s}^{-1}$	
Liquid water flux driven by the gradient of matric potential	q_{LT}	$\text{kg m}^{-2} \text{s}^{-1}$	
Liquid water flux driven by the gradient of air pressure	q_{La}	$\text{kg m}^{-2} \text{s}^{-1}$	
Water vapor flux driven by the gradient of matric potential	q_{Vh}	$\text{kg m}^{-2} \text{s}^{-1}$	
Water vapor flux driven by the gradient of matric potential	q_{VT}	$\text{kg m}^{-2} \text{s}^{-1}$	
Water vapor flux driven by the gradient of air pressure	q_{Va}	$\text{kg m}^{-2} \text{s}^{-1}$	
Mixed pore-air pressure	P_g	Pa	
Specific weight of water	γ_W	$\text{kg m}^{-2} \text{s}^{-2}$	
Transport coefficient for adsorbed liquid flow due to temperature gradient	D_{TD}	$\text{kg m}^{-1} \text{s}^{-1} \text{ } ^\circ\text{C}^{-1}$	
Isothermal vapor conductivity	D_{Vh}	$\text{kg m}^{-2} \text{s}^{-1}$	
Thermal vapor diffusion coefficient	D_{VT}	$\text{kg m}^{-1} \text{s}^{-1} \text{ } ^\circ\text{C}^{-1}$	
Advective vapor transfer coefficient	D_{Va}	s	
Specific heat capacity of dry air	C_a	$\text{J kg}^{-1} \text{ } ^\circ\text{C}^{-1}$	1.005
Liquid water flux	q_L	$\text{kg m}^{-2} \text{s}^{-1}$	
Vapor water flux	q_V	$\text{kg m}^{-2} \text{s}^{-1}$	
Dry air flux	q_a	$\text{kg m}^{-2} \text{s}^{-1}$	
Porosity	ε	-	
Density of dry air	ρ_{da}	kg m^{-3}	
Degree of saturation in the soil	S_L	-	$=\theta_L/\varepsilon$
Degree of air saturation in the soil	S_a	-	$=1-S_L$
Henry's constant	H_e	-	0.02
Molecular diffusivity of water vapor in soil	D_e	$\text{m}^2 \text{s}^{-1}$	
Intrinsic air permeability	K_g	m^2	
Air viscosity	μ_a	$\text{kg m}^{-2} \text{s}^{-1}$	
Volumetric fraction of dry air in the soil	θ_a	$\text{m}^3 \text{m}^{-3}$	$=\theta_V$
Gas phase longitudinal dispersion coefficient	D_{Vg}	$\text{m}^2 \text{s}^{-1}$	
Soil saturated hydraulic conductivity	K_s	m s^{-1}	
Saturated soil water content	θ_s	$\text{m}^3 \text{m}^{-3}$	
Residual soil water content	θ_r	$\text{m}^3 \text{m}^{-3}$	
Air entry value of soil	α	m^{-1}	



Van Genuchten fitting parameters	n	-	
Apparent heat capacity	C_{app}	$\text{J kg}^{-1} \text{ } ^\circ\text{C}^{-1}$	$= C_{soil} + \rho_i \frac{L_f^2}{gT} \frac{d\theta}{d\psi}$
Latent heat flux density	S_h	W m^{-3}	$= -\rho_w L \partial q_v / \partial z$

320



Reference

- Burke, E. J., Jones, C. D., and Koven, C. D.: Estimating the Permafrost-Carbon Climate Response in the CMIP5 Climate Models Using a Simplified Approach, *J. Clim.*, 26, 4897-4909, 10.1175/jcli-d-12-00550.1, 2013.
- 325 Cheng, G., and Wu, T.: Responses of permafrost to climate change and their environmental significance, Qinghai-Tibet Plateau, *Journal of Geophysical Research: Earth Surface*, 112, 10.1029/2006JF000631, 2007.
- Cuntz, M., and Haverd, V.: Physically Accurate Soil Freeze-Thaw Processes in a Global Land Surface Scheme, *Journal of Advances in Modeling Earth Systems*, 10, 54-77, 10.1002/2017MS001100, 2018.
- De Vries, D. A.: Simultaneous transfer of heat and moisture in porous media, *Eos, Transactions American Geophysical Union*, 39, 909-916, 10.1029/TR039i005p00909, 1958.
- 330 De Vries, D. A.: The theory of heat and moisture transfer in porous media revisited, *International Journal of Heat and Mass Transfer*, 30, 1343-1350, [https://doi.org/10.1016/0017-9310\(87\)90166-9](https://doi.org/10.1016/0017-9310(87)90166-9), 1987.
- Dente, L., Vekerdy, Z., Wen, J., and Su, Z.: Maqu network for validation of satellite-derived soil moisture products, *Int. J. Appl. Earth Obs. Geoinf.*, 17, 55-65, 10.1016/j.jag.2011.11.004, 2012.
- 335 Flerchinger, G. N., and Saxton, K. E.: Simultaneous heat and water model of a freezing snow-residue-soil system. I. Theory and development, *Transactions of the American Society of Agricultural Engineers*, 32, 565-571, 1989.
- Guymon, G. L., and Luthin, J. N.: A coupled heat and moisture transport model for Arctic soils, *Water Resour. Res.*, 10, 995-1001, 10.1029/WR010i005p00995, 1974.
- 340 Hansson, K., Šimůnek, J., Mizoguchi, M., Lundin, L. C., and van Genuchten, M. T.: Water flow and heat transport in frozen soil: Numerical solution and freeze-thaw applications, *Vadose Zone J.*, 3, 693-704, 2004.
- Harlan, R. L.: Analysis of coupled heat-fluid transport in partially frozen soil, *Water Resour. Res.*, 9, 1314-1323, 10.1029/WR009i005p01314, 1973.
- Hinzman, L. D., Deal, C. J., McGuire, A. D., Mernild, S. H., Polyakov, I. V., and Walsh, J. E.: Trajectory of the Arctic as an integrated system, *Ecological Applications*, 23, 1837-1868, 10.1890/11-1498.1, 2013.
- 345 Kevin, S., Hugues, L., Vladimir, E. R., Edward, A. G. S., and Ronald, W.: The impact of the permafrost carbon feedback on global climate, *Environmental Research Letters*, 9, 085003, 2014.
- Koren, V., Schaake, J., Mitchell, K., Duan, Q. Y., Chen, F., and Baker, J. M.: A parameterization of snowpack and frozen ground intended for NCEP weather and climate models, *Journal of Geophysical Research Atmospheres*, 104, 19569-19585, 1999.
- 350 Kurylyk, B. L., and Watanabe, K.: The mathematical representation of freezing and thawing processes in variably-saturated, non-deformable soils, *Adv. Water Resour.*, 60, 160-177, 10.1016/j.advwatres.2013.07.016, 2013.
- Li, Q., Sun, S., and Xue, Y.: Analyses and development of a hierarchy of frozen soil models for cold region study, *Journal of Geophysical Research Atmospheres*, 115, 10.1029/2009JD012530, 2010.
- 355 Milly, P. C. D.: Moisture and heat transport in hysteretic, inhomogeneous porous media: A matric head-based formulation and a numerical model, *Water Resour. Res.*, 18, 489-498, 10.1029/WR018i003p00489, 1982.
- Niu, G. Y., Yang, Z. L., Mitchell, K. E., Chen, F., Ek, M. B., Barlage, M., Kumar, A., Manning, K., Niyogi, D., and Rosero, E.: The community Noah land surface model with multiparameterization options (Noah-MP): 1. Model description and evaluation with local-scale measurements, *Journal of Geophysical Research: Atmospheres*, 116, 2011.
- 360 Novak, M. D.: Dynamics of the near-surface evaporation zone and corresponding effects on the surface energy balance of a drying bare soil, *Agr. Forest Meteorol.*, 150, 1358-1365, <https://doi.org/10.1016/j.agrformet.2010.06.005>, 2010.
- 365 Painter, S. L.: Three-phase numerical model of water migration in partially frozen geological media: Model formulation, validation, and applications, *Comput. Geosci.*, 15, 69-85, 10.1007/s10596-010-9197-z, 2011.
- Philip, J. R., and Vries, D. A. D.: Moisture movement in porous materials under temperature gradients, *Eos, Transactions American Geophysical Union*, 38, 222-232, 10.1029/TR038i002p00222, 1957.
- Prunty, L., and Bell, J.: Infiltration Rate vs. Gas Composition and Pressure in Soil Columns *Soil Sci. Soc. Am. J.*, 71, 1473-1475, 10.2136/sssaj2007.0072N, 2007.
- 370 Saito, H., Šimůnek, J., and Mohanty, B. P.: Numerical Analysis of Coupled Water, Vapor, and Heat Transport in the Vadose Zone, *Vadose Zone J.*, 5, 784-800, 10.2136/vzj2006.0007, 2006.



- Schuur, E. A. G., McGuire, A. D., Schädel, C., Grosse, G., Harden, J. W., Hayes, D. J., Hugelius, G., Koven, C. D., Kuhry, P., Lawrence, D. M., Natali, S. M., Olefeldt, D., Romanovsky, V. E., Schaefer, K., Turetsky, M. R., Treat, C. C., and Vonk, J. E.: Climate change and the permafrost carbon feedback, *Nature*, 520, 171-179, 10.1038/nature14338, 2015.
- 375 Su, Z., Wen, J., Dente, L., van der Velde, R., Wang, L., Ma, Y., Yang, K., and Hu, Z.: The Tibetan Plateau observatory of plateau scale soil moisture and soil temperature (Tibet-Obs) for quantifying uncertainties in coarse resolution satellite and model products, *Hydrol. Earth Syst. Sci.*, 15, 2303-2316, 10.5194/hess-15-2303-2011, 2011.
- 380 Su, Z., de Rosnay, P., Wen, J., Wang, L., and Zeng, Y.: Evaluation of ECMWF's soil moisture analyses using observations on the Tibetan Plateau, *Journal of Geophysical Research: Atmospheres*, 118, 5304-5318, 10.1002/jgrd.50468, 2013.
- Subin, Z. M., Koven, C. D., Riley, W. J., Torn, M. S., Lawrence, D. M., and Swenson, S. C.: Effects of Soil Moisture on the Responses of Soil Temperatures to Climate Change in Cold Regions, *J. Clim.*, 26, 3139-3158, 10.1175/jcli-d-12-00305.1, 2013.
- 385 Swenson, S. C., Lawrence, D. M., and Lee, H.: Improved simulation of the terrestrial hydrological cycle in permafrost regions by the Community Land Model, *Journal of Advances in Modeling Earth Systems*, 4, 10.1029/2012MS000165, 2012.
- 390 Touma, J., and Vauclin, M.: Experimental and numerical analysis of two-phase infiltration in a partially saturated soil, *Transport in Porous Media*, 1, 27-55, 10.1007/bf01036524, 1986.
- Viterbo, P., Beljaars, A., Mahfouf, J.-F., and Teixeira, J.: The representation of soil moisture freezing and its impact on the stable boundary layer, *Q. J. Roy. Meteorol. Soc.*, 125, 2401-2426, 10.1002/qj.49712555904, 1999.
- 395 Walvoord, M. A., and Kurylyk, B. L.: Hydrologic Impacts of Thawing Permafrost-A Review, *Vadose Zone J.*, 15, 10.2136/vzj2016.01.0010, 2016.
- Wang, C., and Yang, K.: A New Scheme for Considering Soil Water-Heat Transport Coupling Based on Community Land Model: Model Description and Preliminary Validation, *Journal of Advances in Modeling Earth Systems*, 10, 927-950, 10.1002/2017ms001148, 2018.
- 400 Wicky, J., and Hauck, C.: Numerical modelling of convective heat transport by air flow in permafrost talus slopes, *The Cryosphere*, 11, 1311-1325, 10.5194/tc-11-1311-2017, 2017.
- Yu, L., Zeng, Y., Wen, J., and Su, Z.: Liquid-Vapor-Air Flow in the Frozen Soil, *Journal of Geophysical Research: Atmospheres*, 123, 7393-7415, 10.1029/2018jd028502, 2018.
- 405 Yu, L., Zeng, Y., Faticchi, S., and Su, Z.: How vadose zone mass and energy transfer physics affects the ecohydrological dynamics of a Tibetan meadow?, *The Cryosphere Discuss.*, 2020, 1-31, 10.5194/tc-2020-88, 2020.
- Zeng, Y., Su, Z., Wan, L., and Wen, J.: A simulation analysis of the advective effect on evaporation using a two-phase heat and mass flow model, *Water Resour. Res.*, 47, W10529, 10.1029/2011WR010701, 2011a.
- 410 Zeng, Y., Su, Z., Wan, L., and Wen, J.: Numerical analysis of air-water-heat flow in unsaturated soil: Is it necessary to consider airflow in land surface models?, *Journal of Geophysical Research: Atmospheres*, 116, D20107, 10.1029/2011JD015835, 2011b.
- Zeng, Y., Su, Z., van der Velde, R., Wang, L., Xu, K., Wang, X., and Wen, J.: Blending Satellite Observed, Model Simulated, and in Situ Measured Soil Moisture over Tibetan Plateau, *Remote Sensing*, 8, 268, 2016.
- 415 Zeng, Y. J., and Su, Z. B.: STEMMUS : Simultaneous Transfer of Energy, Mass and Momentum in Unsaturated Soil, ISBN: 978-90-6164-351-7, University of Twente, Faculty of Geo-Information and Earth Observation (ITC), Enschede, 2013.
- Zhao, H., Zeng, Y., Lv, S., and Su, Z.: Analysis of Soil Hydraulic and Thermal Properties for Land Surface Modelling over the Tibetan Plateau, *Earth Syst. Sci. Data Discuss.*, 2018, 1-40, 10.5194/essd-2017-122, 2018.
- 420 Zhao, L., Hu, G., Zou, D., Wu, X., Ma, L., Sun, Z., Yuan, L., Zhou, H., and Liu, S.: Permafrost Changes and Its Effects on Hydrological Processes on Qinghai-Tibet Plateau, *Bulletin of Chinese Academy of Sciences*, 34, 1233-1246, 2019.
- Zheng, D., Velde, R. v. d., Su, Z., Booij, M. J., Hoekstra, A. Y., and Wen, J.: Assessment of Roughness Length Schemes Implemented within the Noah Land Surface Model for High-Altitude Regions, *J. Hydrometeorol.*, 15, 921-937, 10.1175/jhm-d-13-0102.1, 2014.
- 425 Zheng, D., Van der Velde, R., Su, Z., Wang, X., Wen, J., Booij, M. J., Hoekstra, A. Y., and Chen, Y.: Augmentations to the Noah Model Physics for Application to the Yellow River Source Area. Part I: Soil Water Flow, *J. Hydrometeorol.*, 16, 2659-2676, 10.1175/JHM-D-14-0198.1, 2015.



Tables and Figures

430 **Table 1. Governing equations for different complexity of water and heat coupling physics (See appendix for notations)**

Models	Governing equations (water, heat and air)	Number
unCPLD	$\frac{\partial \theta}{\partial t} = -\frac{\partial q}{\partial z} - S = \rho_L \frac{\partial}{\partial z} \left[K \left(\frac{\partial \psi}{\partial z} + 1 \right) \right] - S$	(1)
	$C_{soil} \frac{\partial T}{\partial t} - \rho_i L_f \frac{\partial \theta_i}{\partial t} = \frac{\partial}{\partial z} \left(\lambda_{eff} \frac{\partial T}{\partial z} \right)$	(2)
CPLD	$\frac{\partial}{\partial t} (\rho_L \theta_L + \rho_V \theta_V + \rho_i \theta_i) = -\frac{\partial}{\partial z} (q_L + q_V) - S$	(3)
	$= -\frac{\partial}{\partial z} (q_{Lh} + q_{LT} + q_{Vh} + q_{VT}) - S$	
	$= \rho_L \frac{\partial}{\partial z} \left[K_{Lh} \left(\frac{\partial \psi}{\partial z} + 1 \right) + K_{LT} \frac{\partial T}{\partial z} \right] + \frac{\partial}{\partial z} \left[D_{Vh} \frac{\partial \psi}{\partial z} + D_{VT} \frac{\partial T}{\partial z} \right] - S$	
	$\frac{\partial}{\partial t} [(\rho_s \theta_s C_s + \rho_L \theta_L C_L + \rho_V \theta_V C_V + \rho_i \theta_i C_i)(T - T_r) + \rho_V \theta_V L_0 - \rho_i \theta_i L_f] - \rho_L W \frac{\partial \theta_L}{\partial t}$	
	$= \frac{\partial}{\partial z} \left(\lambda_{eff} \frac{\partial T}{\partial z} \right) - \frac{\partial}{\partial z} [q_L C_L (T - T_r) + q_V (L_0 + C_V (T - T_r))] - C_L S (T - T_r)$	(4)
CPLD-AIR	$\frac{\partial}{\partial t} (\rho_L \theta_L + \rho_V \theta_V + \rho_i \theta_{ice}) = -\frac{\partial}{\partial z} (q_{Lh} + q_{LT} + q_{La} + q_{Vh} + q_{VT} + q_{Va}) - S$	(5)
	$= \rho_L \frac{\partial}{\partial z} \left[K \left(\frac{\partial \psi}{\partial z} + 1 \right) + D_{Td} \frac{\partial T}{\partial z} + \frac{K}{\gamma_w} \frac{\partial P_g}{\partial z} \right] + \frac{\partial}{\partial z} \left[D_{Vh} \frac{\partial \psi}{\partial z} + D_{VT} \frac{\partial T}{\partial z} + D_{Va} \frac{\partial P_g}{\partial z} \right] - S$	
	$\frac{\partial}{\partial t} [(\rho_s \theta_s C_s + \rho_L \theta_L C_L + \rho_V \theta_V C_V + \rho_{da} \theta_a C_a + \rho_i \theta_i C_i)(T - T_r) + \rho_V \theta_V L_0 - \rho_i \theta_i L_f] - \rho_L W \frac{\partial \theta_L}{\partial t}$	
	$= \frac{\partial}{\partial z} \left(\lambda_{eff} \frac{\partial T}{\partial z} \right) - \frac{\partial}{\partial z} [q_L C_L (T - T_r) + q_V (L_0 + C_V (T - T_r)) + q_a C_a (T - T_r)] - C_L S (T - T_r)$	(6)
	$\frac{\partial}{\partial t} [\varepsilon \rho_{da} (S_a + H_c S_L)]$	(7)
	$= \frac{\partial}{\partial z} \left[D_e \frac{\partial \rho_{da}}{\partial z} + \rho_{da} \frac{S_a K_g}{\mu_a} \frac{\partial P_g}{\partial z} - H_c \rho_{da} \frac{q_L}{\rho_L} + (\theta_a D_{Vg}) \frac{\partial \rho_{da}}{\partial z} \right]$	



Table 2. The adopted average values of soil texture and hydraulic properties at different depths (See appendix for notations)

Soil depth (cm)	Clay (%)	Sand (%)	K_s (10^{-6} m s $^{-1}$)	θ_s ($m^3 m^{-3}$)	θ_t ($m^3 m^{-3}$)	α (m^{-1})	n
5-10	9.00	44.13	1.45	0.50	0.035	0.041	1.332
10-40	10.12	44.27	0.94	0.45	0.039	0.041	1.362
40-160	5.59	65.55	0.68	0.41	0.045	0.075	1.590

435

Table 3. Comparative statistics values of observed and simulated soil temperature/moisture with three models, with the bold fonts indicating the best statistical performance

Experiment	Statistics	Soil temperature ($^{\circ}C$)					Soil moisture ($m^3 m^{-3}$)				
		5cm	10cm	20cm	40cm	80cm	5cm	10cm	20cm	40cm	80cm
unCPLD	BIAS	-0.039	0.177	-0.022	-1.103	-0.140	0.009	0.009	0.005	0.004	0.002
	RMSE	0.381	0.407	0.521	1.524	0.526	0.025	0.022	0.031	0.032	0.012
CPLD	BIAS	-0.183	0.093	0.001	-0.956	0.027	0.000	0.004	0.001	0.005	0.001
	RMSE	0.365	0.314	0.186	1.168	0.128	0.008	0.007	0.003	0.007	0.002
CPLD-AIR	BIAS	-0.187	0.093	0.005	-0.953	0.029	-0.001	0.004	0.001	0.005	0.001
	RMSE	0.362	0.316	0.180	1.168	0.126	0.011	0.006	0.003	0.007	0.002

Note: $BIAS = \frac{\sum_{i=1}^n (y_i - \hat{y}_i)}{n}$, $RMSE = \sqrt{\frac{\sum_{i=1}^n (y_i - \hat{y}_i)^2}{n}}$, where y_i , \hat{y}_i are the measured and model simulated soil temperature/moisture; n is the number of data points.

440

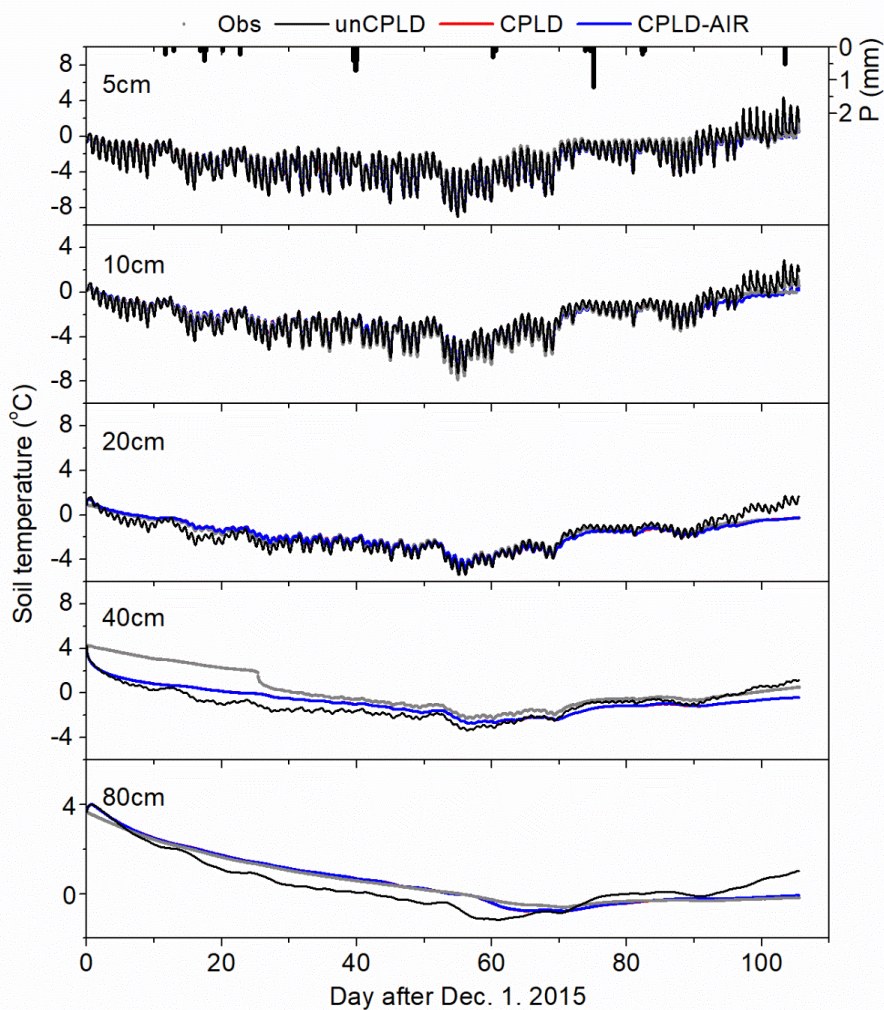
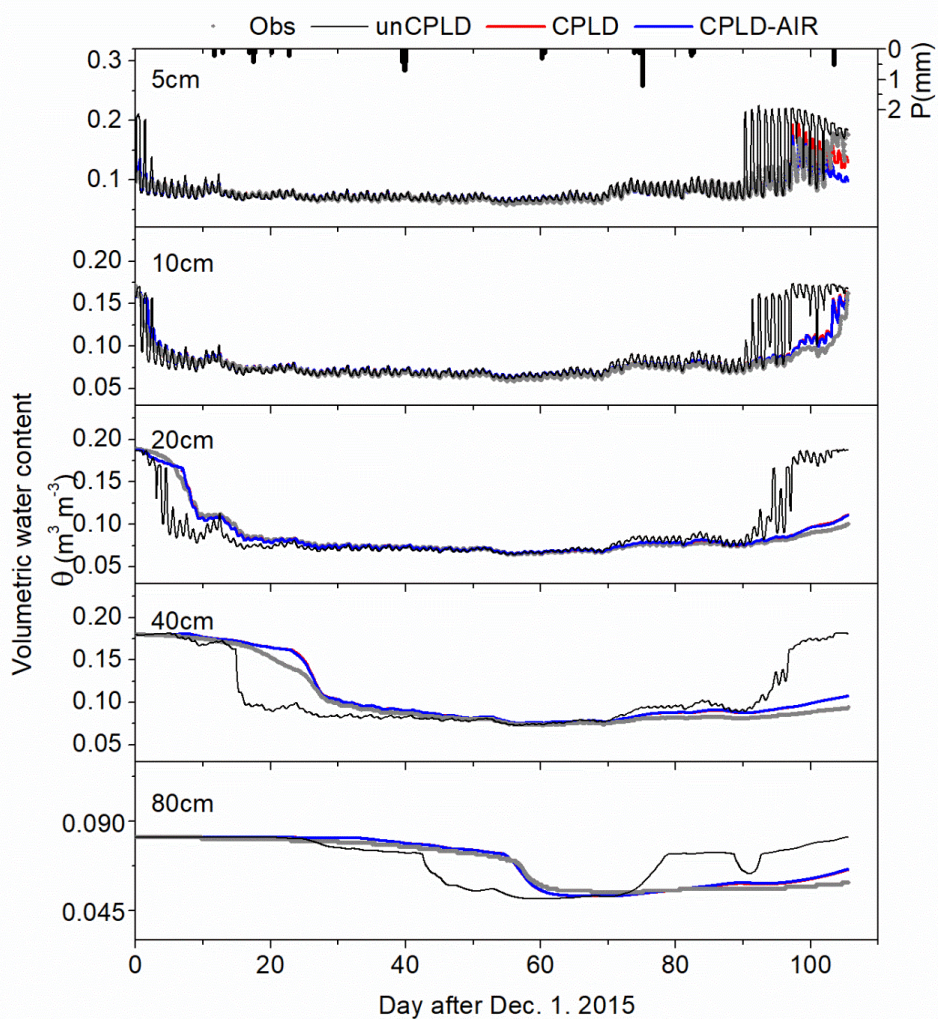
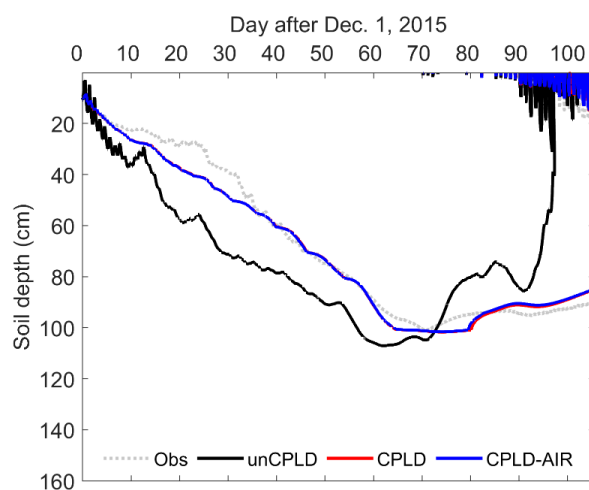


Figure 1. Comparison of measured (Obs) and estimated time series of soil temperature at various soil layers using uncoupled soil physics (unCPLD), coupled water and heat physics (CPLD) and coupled water and heat physics with air flow (CPLD-AIR) model.

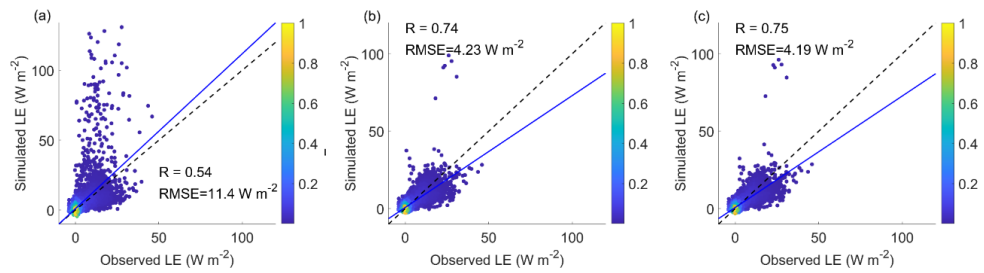


445

Figure 2. Comparison of measured (Obs) and model simulated time series of soil moisture at various soil layers using uncoupled soil physics (unCPLD), coupled water and heat physics (CPLD) and coupled water and heat physics with air flow (CPLD-AIR) model.



450 **Figure 3.** Comparison of measured (Obs) and model simulated freezing front propagation (FFP) using uncoupled soil physics (unCPLD), coupled water and heat physics (CPLD) and coupled water and heat physics with air flow (CPLD-AIR) model. Note the measured FFP was seen as the development of zero degree isothermal lines from the measured soil temperature field.



455 **Figure 4. Scatter plot of observed and model estimated half-hourly latent heat flux using (a) uncoupled soil physics (unCPLD), (b) coupled water and heat physics (CPLD) and (c) coupled water and heat physics with air flow (CPLD-AIR) model. The color indicates the data composite of surface latent heat flux.**

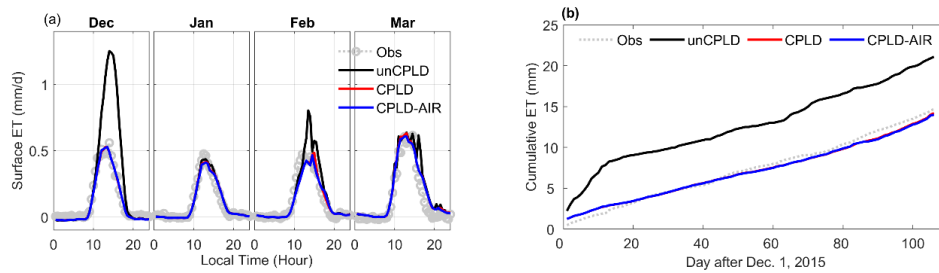
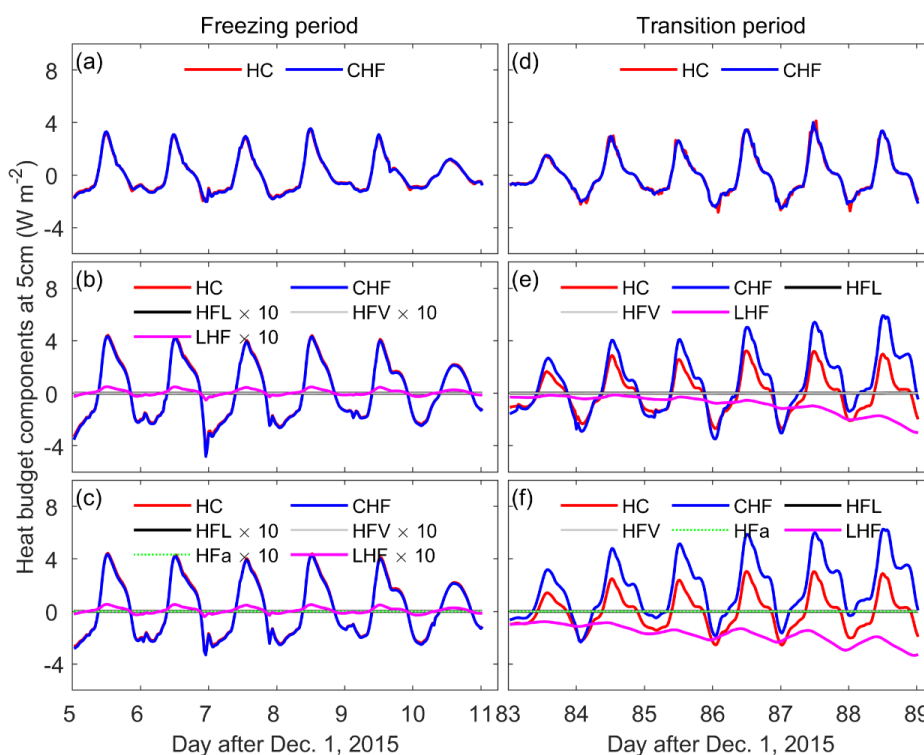
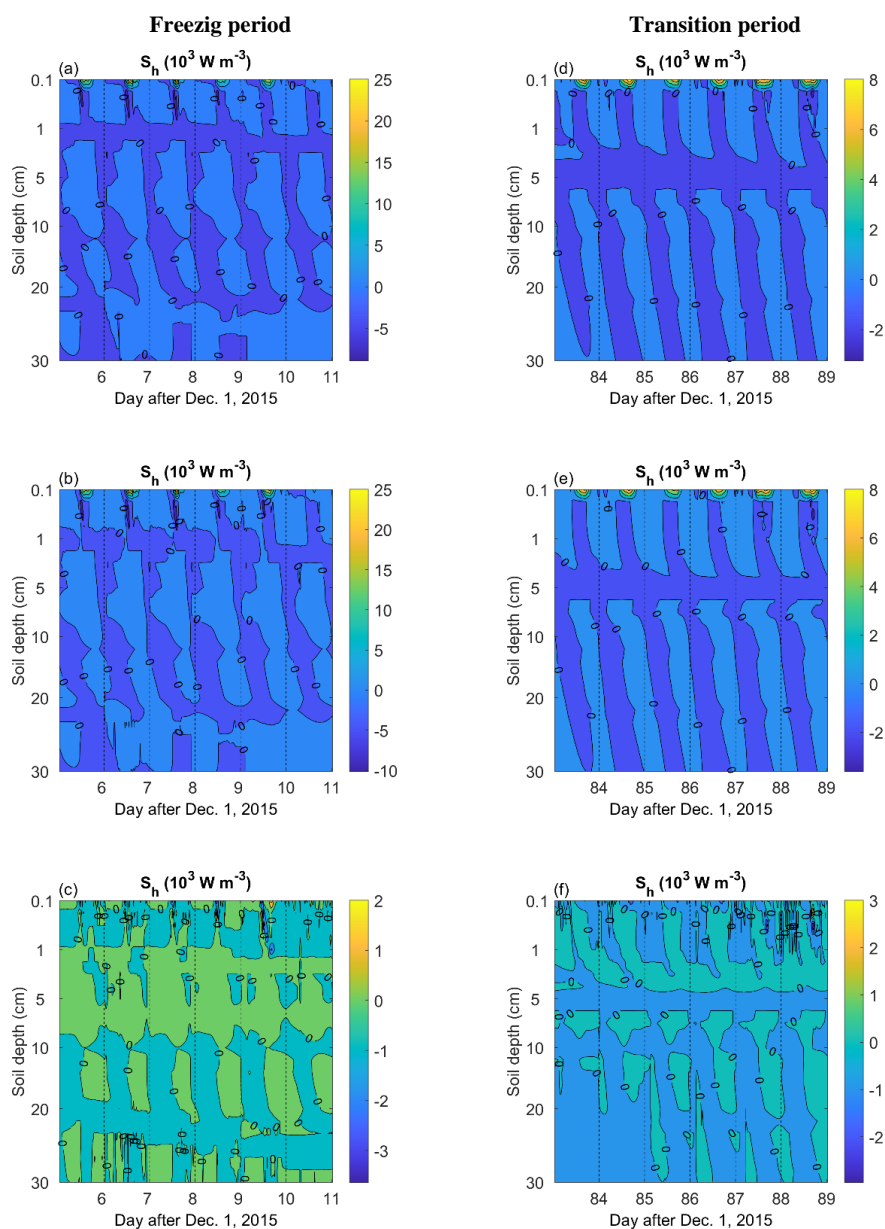


Figure 5. Comparison of observed and model simulated (a) mean diurnal variations of surface evapotranspiration and (b) cumulative evapotranspiration (ET) by unCPLD, CPLD, and CPLD-AIR model.



460 **Figure 6.** Time series of model simulated heat budget components at the soil depth of 5cm using (a & d) unCPLD,
 (b & e) CPLD, and (c & f) CPLD-AIR simulations during the typical 6-day freezing (left column) and freezing-
 465 thawing transition (right column) periods. HC, rate of change of heat content, CHF, conductive heat flux
 divergence, HFL, convective heat flux divergence due to liquid water flow, HFV, convective heat flux divergence
 due to water vapor flow, HFa, convective heat flux divergence due to air flow, LHF, latent heat flux divergence.
 Note that for graphical purposes, HFL, HFV, HFa, and LHF were enhanced by a factor of 10 during the freezing
 period.



470 **Figure 7.** The spatial and temporal distributions of model estimated soil latent heat flux density using (a & d) CPLD, (b & e) CPLD-AIR and (c & f) the difference between CPLD and CPLD-AIR simulations ($S_{h,CPLD-AIR} - S_{h,CPLD}$) during the typical 6-day freezing and freezing-thawing transition periods. The left and right column are for the freezing and freezing-thawing transition period, respectively. Note that figures for the uncPLD model are absent as it can not simulate the subsurface soil latent heat flux density.